Differential and total cross sections of noncapture breakup reactions in the ^{6}Li+^{144}Sm system

D. Martinez Heimann,[1,2,*] A. J. Pacheco,[1,2] O. A. Capurro,[1] A. Arazi,[1,2] C. Balpardo,[1] M. A. Cardona,[1,2,3] P. F. F. Carnelli,[1,2,3] E. de Barbará,[1] J. O. Fernández Niello,[1,2,3] J. M. Figueira,[1,2] D. Hojman,[1,2] G. V. Martí,[1] A. E. Negri,[1,2] and D. Rodrígues[1,2]

[1]*Departamento de Física, TANDAR, Comisión Nacional de Energía Atómica, Av. Gral. Paz 1499, BKNA1650 San Martín, Argentina*

[2]*CONICET, Av. Rivadavia 1917, C1033AAJ Buenos Aires, Argentina*

[3]*Universidad Nacional de General San Martín, Ayacucho 2197, BKNA1650 San Martín, Argentina*

(Received 6 August 2013; revised manuscript received 13 November 2013; published 28 January 2014)

The breakup of the projectile-like fragments in reactions induced by ^{6}Li beams on a ^{144}Sm target at energies close to the Coulomb barrier has been measured through the coincident detection of the emitted light particles. The emphasis of the measurements and the data analysis were placed in the complete characterization of the α-deuteron breakup mode by means of the identification of the breakup fragments and the determination of the total Q value, relative energy of the breakup products, and the angular distribution of their emission. Within the ranges of these variables covered by the present measurements, the results for the $^{6}\mathrm{Li}\rightarrow d+\alpha$ mode show a clear dominance of the resonant channel through the 3^{+} state at 2.186 MeV over other resonant and nonresonant channels. Differential cross sections as a function of the center-of-mass angles of the intermediate binary collision and of the breakup emission, as well as integrated cross sections as a function of energy, have been obtained. The data are compared with those measured for competing processes in the same system and with the results of calculations based on a dynamic classical model that describes noncapture breakup, incomplete fusion, and complete fusion.

DOI: 10.1103/PhysRevC.89.014615 PACS number(s): 25.60.Gc, 25.70.Ef, 25.70.Mn, 25.70.Pq

I. INTRODUCTION

Breakup processes play a fundamental role among the various reactions that can take place in collisions that involve loosely bound nuclei. The experimental evidence for such mechanisms, as well as the general framework for its theoretical interpretation, dates back several decades [1–5]. The interest and motivation for the study of breakup recognizes quite a few—although not totally unrelated—origins. The availability in the past several years of unstable projectiles in numerous laboratories around the world has reinforced the interest for a better understanding of breakup processes, which are likely to occur precisely due to the weak binding of these nuclei.

One line of research deals with the connection between breakup and other reaction channels in the vicinity of the Coulomb barrier. In particular, the relationship between breakup and fusion has been studied both experimentally [6–8] and theoretically [9–13] with focus on the much-debated issue of whether breakup enhances or hinders the occurrence of fusion and under which conditions one or the other effect might prevail. Another motivation for the measurement of breakup reactions has been its use as an indirect tool for the study of inverse radiative capture reactions of astrophysical interest via the detailed balance principle [14]. This application usually involves measurements of reactions that occur just above the breakup threshold, thus requiring the use of appropriate experimental techniques for the detection of the coincident breakup products that are emitted within cones of extremely small opening angles [15,16].

Finally, the mechanism that underlies breakup reactions and their characterization is in itself a matter of interest. The lack of more extensive and detailed information on this question relates to experimental limitations and/or to the incomplete information that can be derived from inclusive experiments, from which energy and angular distributions of light particles can be obtained although with little or indirect reference to the exact source of emission. The achievement of a complete experimental characterization of the mechanism may require exclusive measurements and the interpretation of the results in terms of physically significant coordinates. One of the aspects related to the reaction mechanism is the determination of the sequential or direct character of the observed breakup reactions and the experimental fingerprints of each one of those processes [17,18]. Another point relates to the angular distributions of the fragments emitted in a breakup reaction measured in the relevant center-of-mass (c.m.) reference frames [19,20]. The occurrence of more complex mechanisms in which breakup is actually just one stage in a sequence [5,21,22] is also particularly intriguing. In this respect, the observation of ^{6}Li breakup as the main contribution in reactions induced by ^{7}Li projectiles has directed the attention to the study of the particular mechanism consisting of neutron transfer followed by the breakup of the projectile-like product [23]. Similar complex processes have also been observed and studied in other systems; the most comprehensive recent experiments involve high-efficiency exclusive measurements of breakup products in reactions of ^{6}Li and ^{7}Li on several targets [24,25].

In this work we report some of the results obtained from coincident measurements of the light particles emitted in reactions induced by weakly bound lithium projectiles on the spherical ^{144}Sm target. More specifically, we focus our attention on the reactions that involve the elastic noncapture breakup of the ^{6}Li projectile into a deuteron and an α particle at several bombarding energies, leaving for a separate publication

*diegoheimann@gmail.com

the discussion of the sequential transfer/breakup channel that has also been observed for both ^{6}Li and ^{7}Li projectiles. The results of these exclusive measurements include angular distributions and excitation functions, and they are presented and discussed in terms of the relevant, experimentally deduced, center-of-mass variables that completely describe the three-body exit channel. We study the isotropy of the light-fragment emission in the reference frame of the ejectile that breaks up. Differential and integrated cross sections have been obtained from the data and they are presented in comparison to other reaction channels that have been previously measured for the same system and also to the predictions of a dynamic classical model for the description of breakup reactions [26,27].

II. EXPERIMENTAL SETUP

The experimental work was carried out using the 20-UD tandem accelerator TANDAR. Beams of ^{6}Li with laboratory energies $E_{\rm lab}$ between 23 and 30 MeV and typical intensities in the range 1 to 15 pnA were used to bombard a 96% enriched ^{144}Sm target, approximately 60 μg/cm^2 thick (obtained from Rutherford elastic-scattering measurements). The identification and characterization of the breakup reactions was based on the coincident detection of the produced light particles, for which purpose we have used two silicon ΔE-E telescopes mounted on independent arms inside a 76-cm-diameter scattering chamber, as shown schematically in Fig. 1. The telescope located at the most forward (backward) angle will be referred to in what follows as telescope 1 (telescope 2). The thicknesses were 1 mm for both E detectors and 30 μm (20 μm) for ΔE_1 (ΔE_2). The nominal thicknesses of the dead layers of the ΔE and E detectors, of 0.3 and 0.08 μm, respectively, were found to have a negligible effect on the energy calibrations and on the determination of total energies of all the particles of interest. Various sets of measurements have been performed using either rectangular or circular entrance collimators at different distances between the target and the telescopes. Typical angular acceptances of the detectors were $\Delta\theta_1 \approx \pm 2.5^\circ$ and $\Delta\theta_2 \approx \pm 5^\circ$. In general, the angular separation between telescopes was kept at the minimum possible value compatible with the geometry of the mounts, usually around 17°. At this fixed angular separation, the maximum angular range covered by varying the position of both telescopes was 45° to 135°. The resulting geometrical efficiencies of the various detection configurations, although quite complex, have been calculated in detail (see discussion later) for different breakup channels of interest. It could be shown in particular that the efficiencies for projectile breakup are very similar to those for more complex processes such as breakup of the projectile-like product following transfer. Even though for all of these channels the efficiency is reasonably high over a broad range of relative energies of the (light) breakup products, a few runs at larger angular separations have also been taken to explore other regions of this variable. A separate set of measurements has been done to study out-of-plane correlations using a specific modified mount for telescope 2. The out-of-plane angles covered by this telescope ranges between 0° and 30°. For normalization purposes, two additional solid-state detectors were placed at forward angles (their position varied, through different experiments, between 20° and 30°) to monitor Rutherford elastic scattering.

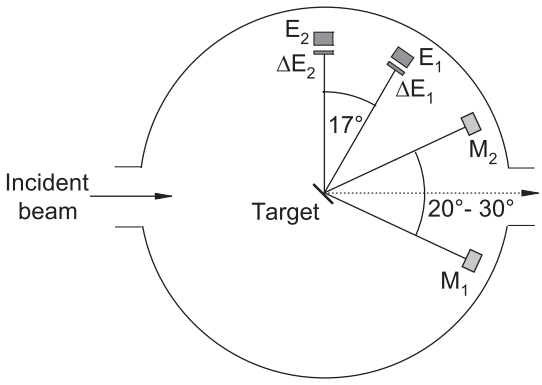

FIG. 1. Schematic of experimental setup for coincidence measurements.

All the detectors were energy calibrated using a combined ^{239}Pu-^{241}Am-^{244}Cm α-emitting source together with the position of the peak in the energy spectrum corresponding to the elastically scattered projectile. The breakup products were detected using standard slow and fast coincidence techniques. The data were acquired as multiparametric events in either singles or coincidence mode. The recorded parameters were proportional to the energies deposited in the four solid-state detectors (ΔE_1, ΔE_2, E_1, and E_2) and the time-of-flight difference (ΔTOF) between the fragments that hit each telescope.

III. DATA REDUCTION

Figure 2 shows two-dimensional residual energy versus energy loss spectra taken in coincidence mode for both telescopes, where clear separation among isotopes with atomic masses $A = 1$ and 2 for $Z = 1$ can be observed for telescope 1. This identification was used in combination with the absolute energy measurements, which took into account corrections for energy losses in the target, to obtain the velocity vectors of each of the coincident breakup products in the laboratory frame of reference. These laboratory angles and velocities were transformed on an event-by-event basis to a set of more physically meaningful variables according to the discussion that follows.

A. Transformation of variables

The complete characterization of collisions leading to three or more final fragments starting from the detection of any two of them (known masses and kinetic energies) is a relatively straightforward problem that has been treated elsewhere. We present here the summary of a few basic points which are relevant for the present work, based on the treatment of Refs. [28,29]. For the sake of simplicity in the notation, we take as an example the reaction ^{6}Li+^{144}Sm$\rightarrow$^{2}H+^{4}He+^{144}Sm (the generalization to other similar channels is straightforward). For this particular case the transformation from laboratory variables to the new set, more adequate for the natural description

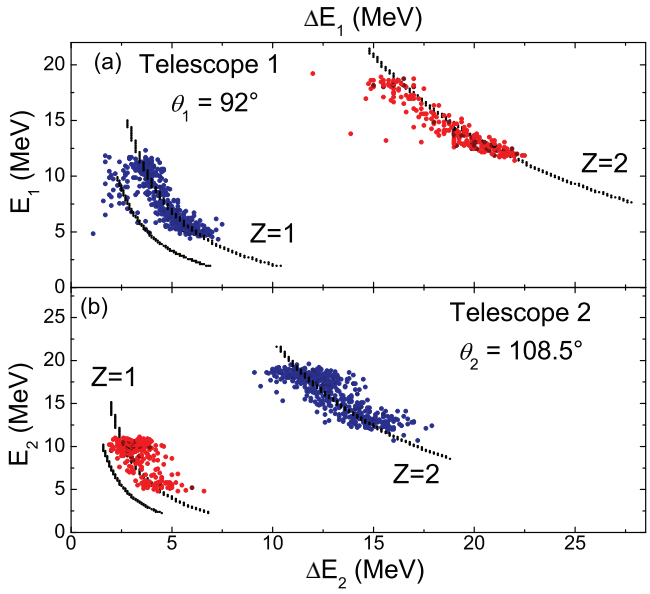

FIG. 2. (Color online) Two-dimensional residual energy vs. energy loss spectra of the light particles emitted in the reaction ^{6}Li (30 MeV)+^{144}Sm, detected in coincidence by both telescopes. The curves are the calculated loci for $Z = 1$, $A = 1,2$ and $Z = 2$, $A = 4$. The colors of the data points correspond to additional gating conditions used to emphasize the different types of coincidences: particles with $Z = 1$ detected by telescope 1 (blue) or telescope 2 (red).

of system, is shown in Fig. 3. The transformation illustrated in this figure finds inspiration in a sequential mechanism consisting of binary scattering, ^{6}Li+^{144}Sm→^{6}Li+^{144}Sm, followed by the breakup of the corresponding projectile-like nucleus, ^{6}Li→^{2}H+^{4}He. This purely kinematical decomposition is always valid and does not require the actual occurrence of neither this particular intermediate binary stage nor of any other mechanism or sequence of events leading to the same observed exit channel. As a matter of fact, any intermediate

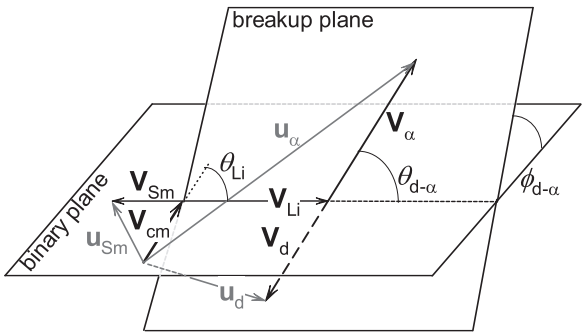

FIG. 3. Diagram of the asymptotic velocities of the emitted fragments in the breakup reaction ^{6}Li+^{144}Sm→^{2}H+^{4}He+^{144}Sm. The planes labeled as "binary" and "breakup" illustrate the decomposition in terms of two virtual stages. The laboratory velocity of particle x is indicated by $\mathbf{u}_x$. The velocity with respect to the appropriate center-of-mass system (^{6}Li-^{144}Sm or d-α) is indicated by $\mathbf{V}_x$. See text for details.

binary partition consisting of (i) one of the final fragments and (ii) the sum of the other two could have, in principle, been chosen for this purpose. Bearing this in mind, the velocity diagram of Fig. 3 shows the asymptotic laboratory velocities of the α particle, deuteron, and ^{144}Sm ($\mathbf{u}_\alpha$, $\mathbf{u}_d$, and $\mathbf{u}_{\rm Sm}$) as the following vector additions:

$$\begin{aligned} \mathbf{u}_\alpha &= \mathbf{V}_{\rm c.m.} + \mathbf{V}_{\rm Li} + \mathbf{V}_\alpha \\ \mathbf{u}_d &= \mathbf{V}_{\rm c.m.} + \mathbf{V}_{\rm Li} + \mathbf{V}_d, \\ \mathbf{u}_{\rm Sm} &= \mathbf{V}_{\rm c.m.} + \mathbf{V}_{\rm Sm} \end{aligned} \tag{1}$$

where $\mathbf{V}_{\rm c.m.}$ is the velocity of the center of mass, $\mathbf{V}_{\rm Li}$ and $\mathbf{V}_{\rm Sm}$ are the velocities of the ^{6}Li and the ^{144}Sm in the center-of-mass system, and $\mathbf{V}_\alpha$, $\mathbf{V}_d$ are the α-particle and deuteron velocities in the ^{6}Li rest frame. All of these vectors can be directly obtained from the raw data. Taking into account the conservation of linear momentum (total kinetic energy is not necessarily conserved) one can reduce the total number of variables needed for a complete description of the system from 9 to 6. According to Fig. 3 and Ref. [17], we choose the following as the final relevant variables: (a) the total reaction Q value, (b) the kinetic energy of the deuteron-α system in the ^{6}Li frame, $E_{d-\alpha}$, (c) the center-of-mass binary scattering emission angles $\theta_{\rm Li}$ and $\phi_{\rm Li}$ (the latter not shown in Fig. 3), and (d) the breakup emission angles $\theta_{d-\alpha}$ and $\phi_{d-\alpha}$. These six variables were obtained through appropriate event-by-event operations using the experimental velocity vectors of Eq. (1). These calculations are affected in general by uncertainties that arise from the finite solid angles subtended by the entrance collimators, thus causing possible distortions in the resulting distributions. This effect will be further discussed and evaluated in connection with the actual data obtained in the present work.

B. Selection of breakup events

After taking into account the appropriate energy calibrations and corrections as mentioned above, the raw data were first transformed into laboratory velocities of the coincident light fragments and finally into the new set of six variables which were saved as additional parameters for each individual event. Distributions of these relevant variables were produced taking advantage of the fact that the event-by-event handling of the raw data automatically takes care of the Jacobian of the transformation. Events that contained true coincidences were selected from 2D correlations between the time-of-flight difference and the residual energy, as illustrated in Fig. 4. The curves have been calculated with the code SUPERKIN [28,29] assuming a uniform yield for all the reactions and kinematical configurations that are detectable by the setup. This means, in terms of the diagram shown in Fig. 3, for all the possible combinations between (i) the center-of-mass angles for the binary reaction, $\theta_{\rm Li}$, and (ii) the center-of-mass angles of the "subsequent" breakup of the projectile-like product, $\theta_{x-\alpha}$ ($x = p$, d, or t), that might result in coincident hits in both detectors. In particular, a range of relative energies of the breakup between 0 and 2 MeV has been assumed. The scatter plot of Fig. 4 illustrates a very low fraction (less than 3%) of random coincidences with respect to true coincidences, in accordance with the overall counting rates and with a typical

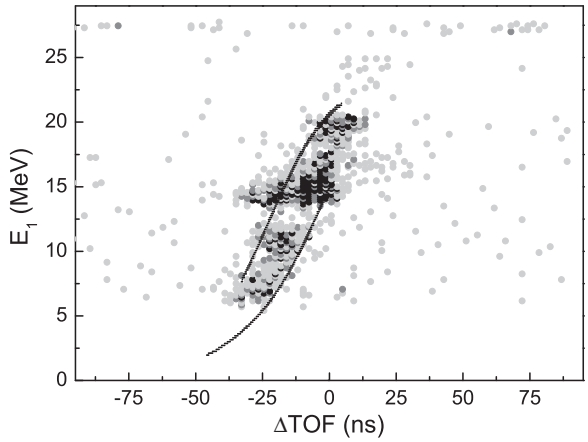

FIG. 4. Two-dimensional E_1 vs ΔTOF spectrum of the light particles detected in coincidence. The displayed residual energy corresponds to telescope 1. The curves have been calculated under the assumption of a broad (0 to 2 MeV) uniform distribution of d-α relative energies.

time resolution of 5 ns. Additional gating conditions were set to require the desired masses of the particles detected in each telescope. This could be done directly from the event-by-event assignment of the corresponding mass numbers A_1 and A_2 whenever the mass resolution for $Z = 1$ was good enough. An alternative or complementary selection procedure was based on two-dimensional E_1 versus E_2 plots which exhibit definite correlations for different geometric configurations of the telescopes. An example is shown in Fig. 5 together with the corresponding SUPERKIN calculation (dashed curve) for a broad distribution of d-α relative energies.

C. Extraction of differential and integrated cross sections

Absolute differential cross sections with respect to the transformed variables have been obtained from the data. For this purpose we have applied a procedure that is based on the following general considerations: Given a generic set

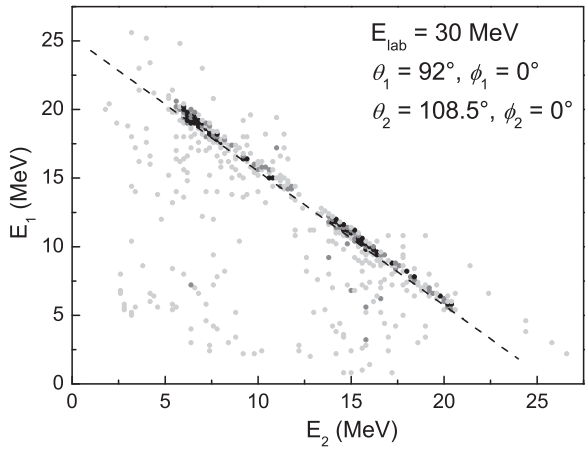

FIG. 5. Experimental correlation between the residual energies recorded in both telescopes. The dashed curve has been calculated under the assumption of a broad distribution of d-α relative energies.

of n variables $Y = \{y_1 \dots y_n\}$, the corresponding nth-fold differential cross section is given by $(d^n\sigma/dy_1 \dots dy_n)$. An ideal experiment to determine this cross section at a fixed point $Y^0 = \{y_1^0 \dots y_n^0\}$ would involve the measurement of the number of events that fall within a cell defined by a set of increments $\Delta Y = \{\Delta y_1 \dots \Delta y_n\}$ centered at that same point. In general, the increments would be chosen taking into account the resolutions of the measurements and the counting statistics involved in a given experiment. Under these circumstances the approximate cross section at Y^0 is given by

$$\frac{d^n\sigma}{dy_1 \dots dy_n} = K\frac{N(Y^0)}{\varepsilon(Y^0)\Delta v}, \tag{2}$$

where $N(Y^0)$ is the number of recorded events in the cell centered at Y^0, $\Delta v \equiv \prod_{j=1}^{n} \Delta y_j$ is the volume of the cell, K is the normalization constant that contains the information on the number of incident projectiles and surface density of the target nuclei, and $\varepsilon(Y_0)$ is the efficiency of the detection system at Y_0.

In our experiments, the set of variables of interest is the one presented in Sec. III A. As discussed, these variables are not directly measured, thus preventing the direct application of Eq. (2). Instead, they are obtained from an event-by-event transformation starting from a set of raw variables $X = \{x_1 \dots x_n\}$ which are the ones directly measured in a coincidence experiment with a rather involved geometric efficiency. Although this problem has been analytically treated [17,30] we have adopted a numerical approach through the use of the code SUPERKIN which calculates the coincidence efficiency taking the exact geometry of the detection device into account. A brief summary of this program is presented in what follows for the sake of understanding its application to the present determination of breakup cross sections. The basic input of the program is the entrance channel, the three-body exit channel (breakup mode) and the detection device (in our case, two telescopes defined by their angular positions in space, thicknesses of the ΔE components, and shape and dimension of the entrance collimators). For fixed values of the relevant Y variables (in our case, the "binary" and "breakup" center-of-mass angles, and the relative energies of the breakup fragments), the corresponding velocity vectors in the laboratory reference frame of all the reaction products are calculated. Then, the incidence of each one of these particles on any of the defined detectors is evaluated. The whole calculation is repeated for all possible values of the angular variables according to a grid that covers $4\pi \times 4\pi$ sr^2, and for all the values of the relative energies within a selected range. We denote the set of bins used in these calculation by $\delta Y = \{\delta y_1 \dots \delta y_n\}$ and the corresponding volume of this calculation cell as $\delta v \equiv \prod_{j=1}^{n} \delta y_j$. The cases that satisfy the selected coincidence requirements (positive events) are recorded sequentially in multiparametric mode, including the corresponding sets of variables X and Y. The experimental differential cross section with respect to the variables of interest Y at Y^0 is finally obtained as

$$\frac{d^n\sigma}{dy_1 \dots dy_n} = J(Y^0)K\frac{N(Y^0)}{N_{SK}\delta v}. \tag{3}$$

Here, N_{SK} is the number of positive events calculated by SUPERKIN in a measurement cell ΔY centered at Y^0. The factor $J(Y^0)$ is a Jacobian (in general its value is very close to one) that takes into account the nonlinear relation between the reconstructed and the "true" values of each variable that may arise as a consequence of finite solid angles of the detectors (it is not the Jacobian of the transformation of variables). In general, from Eqs. (2) and (3) and considering the capabilities of the code, it can be seen that the geometric efficiency for the measurement of three-body processes using a large variety of experimental setups (different spatial configurations of the detectors, different coincidence requirements, circular, rectangular or annular collimators, segmented active areas, etc.) can be readily obtained as

$$\varepsilon(Y) = \frac{N_{SK}\delta\nu}{\Delta\nu}. \quad (4)$$

For the particular case of our experiments, the cross section that could be directly obtained from the data using Eq. (3) is $d^2\sigma/d\Omega_{d-\alpha}d\Omega_{Li}$ as a function of the binary scattering angles θ_{Li}, ϕ_{Li} and the breakup emission angles $\theta_{d-\alpha}$, $\phi_{d-\alpha}$. Lower-order differential cross sections can be obtained from the sum of Eq. (3) over the whole range of the appropriate variables, although in most practical cases these sums should extend well beyond the regions that have reasonably high efficiencies. For our case, in order to obtain the partially integrated cross section $d\sigma/d\Omega_{Li}$ and the total cross section σ, we have incorporated the information contained in the binary and breakup angular distributions that we have measured in the present work as a guide for the required interpolations and extrapolations.

IV. RESULTS

The procedure summarized in Sec. III was applied to obtain spectra of all the significant variables. In Sec. IV A through IV D we present the particular features observed for each one of these variables and, in terms of them, we discuss the physical interpretation of the present experimental results. Finally, in Sec. IV E, we summarize the experimental values of the absolute differential cross sections as well as the results of different assumptions for their integration to obtain total noncapture breakup cross sections.

A. Q values

After selection of deuteron-α coincidences following the previously outlined procedure, Q values have been calculated for each individual event as the difference between the projectile energy and the sum of the kinetic energies of all the fragments in the exit channel. The energies of the light particles were obtained from the measurements, taking into account all the appropriate corrections. The energy of the unobserved heavy fragment was calculated considering momentum conservation. Examples of spectra obtained at three different bombarding energies and at fixed angles of the telescopes ($\theta_1 = 92^\circ$, $\theta_2 = 108.5^\circ$) are presented in Fig. 6. The distributions seem to be consistent with the preferential population of the ground state and, possibly, of the lowest excited states of the target (1.66 and 1.81 MeV) at all measured energies.

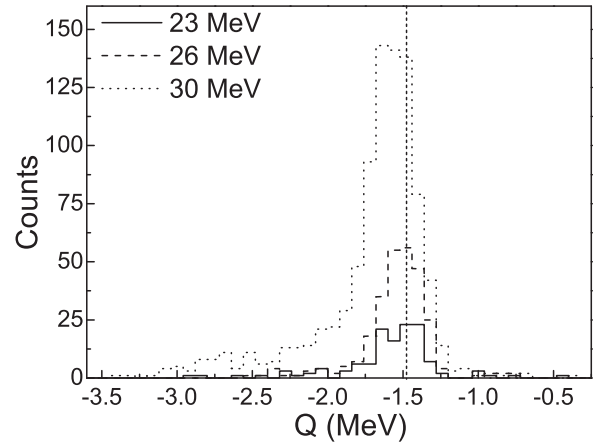

FIG. 6. Q-value spectra obtained at three bombarding energies. The vertical line indicates the value corresponding to the ^{6}Li $\rightarrow d+\alpha$ breakup leading to the ground state.

B. Relative energies

The distribution of relative energies (i.e., kinetic energies of the breakup products in the reference frame of the virtual nucleus that breaks up) is one of the most important features that characterizes the reactions under study. The relative energy spectrum provides additional information on the breakup mechanism [24], specifically, the resonant or direct character of the process. Resonant breakup involving unbound excited states should become apparent through characteristic peaks or bumps in the spectra. On the other hand, nonresonant or direct breakup processes that directly populate the continuum should probably be associated with much less defined structures. Since relative energies are necessarily measured asymptotically, the exact correspondence between a given resonant channel and the characteristics of the corresponding related structure in the distribution is not obvious. In principle, it cannot be predicted unless one models the breakup process in the short distance domain and then follows the evolution to asymptotic distances. Although it has been customary to assume that the asymptotic relative energy is equal to the difference between the excitation energy of the resonant state and the breakup Q value [23,31,32], corrections to this value due to the Coulomb post acceleration of the light breakup products in the field of a heavier partner have been observed and/or calculated under particular model assumptions [15,33]. According to the calculations presented in Ref. [15] the effect is expected to become less important as the breakup takes place at longer distances from the target. In addition, if the charge-to-mass ratios of the breakup fragments and of the nucleus that breaks up are equal (such as in the ^{6}Li$\rightarrow d+\alpha$ case), then no Coulomb shift is predicted.

In view of the above considerations we have undertaken a detailed study of the asymptotic relative energies in our data and use it as a tool to characterize the breakup mechanism. Taking into account Eq. (1), relative energies between the coincident fragments (for example, α particles and deuterons)

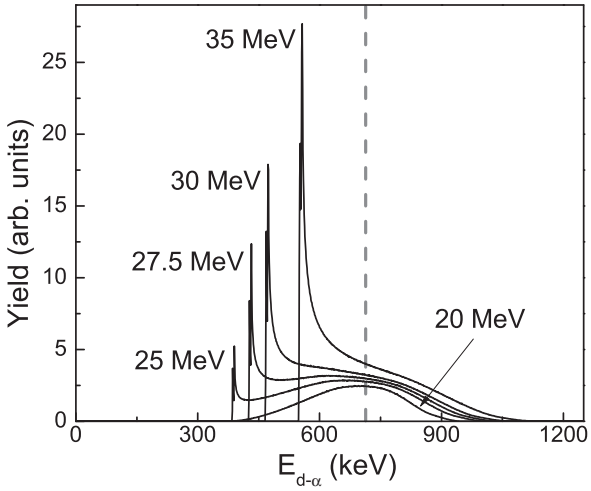

FIG. 7. Calculated distributions of d-α relative energies that simulate the distortions produced by the reconstruction of the actual data. The curves correspond to different projectile energies and they have all been obtained under the assumption of a "true" narrow input distribution in relative energy centered at the value indicated by the vertical dashed line. The calculations reproduce one of the actual geometric configurations that have been used. See text for details.

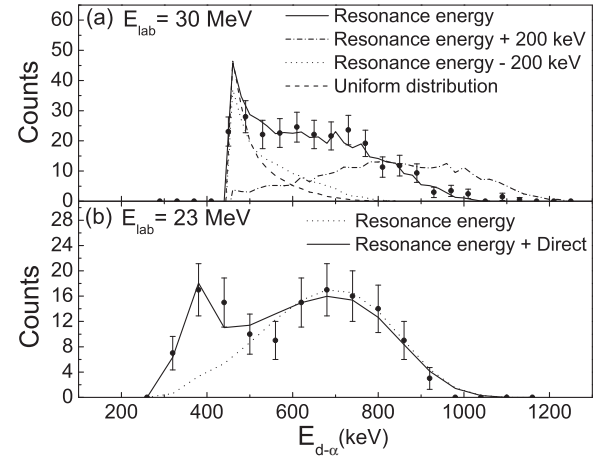

FIG. 8. Experimental and several calculated distorted distributions of d-α relative energies for the events detected in coincidence in the two-telescope system for energies above (a) and below (b) the barrier. In spite of the distortions (see text and Fig. 7) the comparison of the data with the calculations provides information on the actual $E_{d-\alpha}$ distributions. See text for details.

were obtained from each individual event as

$$E_{d-\alpha} = \tfrac{1}{2}(m_d \mathbf{V}_d \cdot \mathbf{V}_d + m_\alpha \mathbf{V}_\alpha \cdot \mathbf{V}_\alpha). \quad (5)$$

For this particular variable the results obtained through the event-by-event application of Eq. (5) should be interpreted with care because, as pointed out in Ref. [17], the extracted values of $E_{d-\alpha}$ are strongly dependent on the opening angle. Therefore the uncertainties in the actual emission angles of the coincident particles due to the large angular acceptances of the detectors produce in most practical cases very large errors in the obtained relative energy values. Figure 7 illustrates the distortion expected from this effect as a function of the bombarding energy. The calculation reproduces the exact geometry of our experimental device for an actual run taken at $\theta_1 = 92.0^\circ$, $\theta_2 = 108.5^\circ$ with angular acceptances $\Delta\theta_1 = \pm 2.8^\circ$ and $\Delta\theta_2 = \pm 4.7^\circ$. To obtain the curves shown we have first run calculations with the code SUPERKIN to simulate the experimental conditions for the ^{6}Li$\rightarrow d$+α channel at five projectile energies as follows: 20, 25, 27.5, 30, and 35 MeV. The resulting event-by-event output file has then been processed with the same analysis programs that are used for the real data. For these calculations we have considered as an example a narrow (20-keV-wide) input distribution in the relative energy, centered at 712 keV, as indicated by the vertical line. In order to simulate the actual experimental limitations in the event-by-event application of Eq. (5), we replace the exact laboratory emission angle of each detected particle by the mean angle of the corresponding telescope. The distortions predicted by this simulation of the actual data analysis present two basic characteristics. On the one hand, a very important broadening, as compared to the narrow input distribution, can be observed. As the bombarding energy increases, there is an additional effect that consists in a progressive "truncation" and accumulation of events at the left end of the calculated spectrum. The resulting sharp cutoff increases with projectile energy and its value at a given bombarding energy is the minimum $E_{d-\alpha}$ that would be detected with ideally small collimators and the telescopes located at the nominal opening angle. Taking these features into account we will show next that, in spite of the huge distortions, the calculated distributions provide valuable information on the actual distributions and therefore allow us to evaluate the resonant or direct character of the breakup reactions under investigation as described below.

We start by studying the highest bombarding energies taking as an example the data for ^{6}Li+^{144}Sm at $E_{\rm lab} =$ 30 MeV at the angular configuration considered in the previous simulations, 92°/108.5°. Figure 8(a) compares the results of applying exactly the same procedure to (i) the data and (ii) the output of various calculations done with the code SUPERKIN for different input distributions. The solid curve (the one that best describes the data points) has been obtained assuming a narrow input distribution centered at an asymptotic relative kinetic energy of 0.712 MeV. Under the previously discussed assumption of no Coulomb shift for this case, this value would correspond to a breakup reaction that proceeds through the first 3^+ resonant state of ^{6}Li located at an excitation energy of 2.186 MeV. The other three curves, which clearly fail to reproduce the experimental behavior, have been included to illustrate the sensitivity of the calculations with respect to changes in the input distribution. Two of them also correspond to narrow distributions but are now arbitrarily centered at energies 200 keV above (dashed-dotted curve) and below (dotted curve) the resonance. Finally, the dashed curve results from a uniform input distribution over the range $E_{d-\alpha} =$ [0,0.63] MeV, i.e., extending from the breakup threshold up to a sharp cutoff at slightly below the kinetic energy that corresponds to the resonance. This last curve has been included as a crude representation of direct, nonresonant

breakup reactions. From the quality of the fit in each case it can be concluded that for the ^{6}Li$\rightarrow d+\alpha$ channel the data are consistent with a strong dominance of resonant breakup over direct breakup. Similar results have been obtained for measurements done at all other angular configurations of the coincident detectors and for the bombarding energies down to 26 MeV.

A substantially different behavior is observed at $E_{\rm lab} = 23$ and 24 MeV, as shown in Fig. 8(b) for the lowest-energy case. Unlike at the highest energies, the experimental points are no longer well described by the calculation that assumes a single resonant peak (dotted curve). This lack of agreement reflects the appearance of an additional nonresonant component characterized by a wide distribution with lower values of $E_{d-\alpha}$. Actually, and more correctly, it should be said (and it can be demonstrated) that as $E_{\rm lab}$ decreases the detection system becomes more efficient for the separation and identification of such component, which may go unobserved at $E_{\rm lab} =$ 26 MeV and above. The solid curve in Fig. 8(b) shows the best fit of the data assuming a linear combination of the resonant component and a uniform distribution of $E_{d-\alpha}$ that extends from 0 MeV to an upper cutoff. The weighting coefficients for the two components have been taken as adjustable parameters. By comparing the quality of the least-squares fits as a function of the upper limit of the uniform distribution (not shown in the figure) we have established that the best representation is obtained with a value 0.5 ± 0.2 MeV. The relative yields for the production of resonant and nonresonant breakup obtained in this way will be presented and discussed in connection with the extraction of absolute cross sections. Further general discussion on the experimental distributions of $E_{d-\alpha}$ is included in what follows.

C. Binary scattering angles

The polar emission angle $\theta_{\rm Li}$ was obtained for each event as follows:

$$\mathbf{V}_{\rm Li} \cdot \mathbf{V}_{\rm c.m.} = V_{\rm Li} V_{\rm c.m.} \cos(\theta_{\rm Li}). \quad (6)$$

Experimental distributions of this angular variable at $E_{\rm lab} =$ 30 MeV are shown in Fig. 9(a). The data points have been obtained according to the procedure described in Sec. III A. The solid curve represents the corresponding geometric efficiency which has been calculated with the code SUPERKIN for the case of resonant breakup, i.e., assuming a narrow distribution of relative energies centered at $E_{d-\alpha} = 0.712$ keV and isotropic emission. The observed structure consists of four peaks, and it can be shown that they correspond to four different groups of kinematical configurations that satisfy the requirement of coincident detection of the resonant-breakup fragments. The calculations predict very accurately the angular position of the experimental peaks and qualitatively describe the general shape of the data; these results reinforce the evidence for the dominant resonant character of the noncapture projectile-breakup reactions observed at the highest bombarding energies. On the other hand, the calculation fails to reproduce the observed relative heights of the peaks which may reflect the inadequacy of assuming isotropic emissions (both for ^{6}Li and for the breakup fragments). The four kinematical

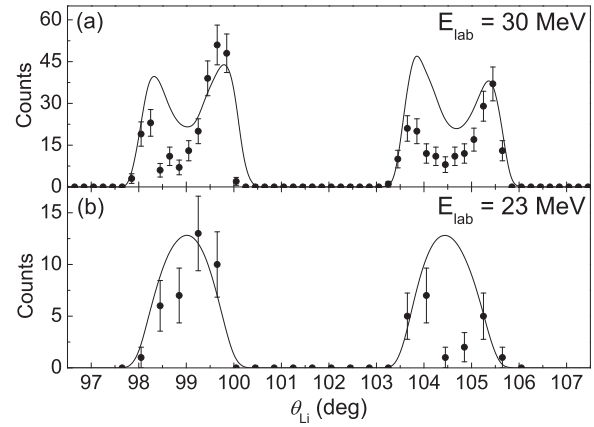

FIG. 9. Experimental and calculated distributions of binary (^{6}Li) asymptotic scattering angles. The data have been taken at $\theta_1 = 92^\circ$ and $\theta_2 = 108.5^\circ$.

configurations have very similar values of the binary angle $\theta_{\rm Li}$ (they differ among each other in a few degrees) and have very different values of the breakup angle $\theta_{d-\alpha}$. Therefore it is likely that the observed asymmetric yields are not caused by the dependence of the emission on $\theta_{\rm Li}$. Instead, one can probably conclude that they actually reflect the anisotropy of the emission of the breakup products in the reference frame of the binary projectile-like fragment. This issue will be discussed specifically in Sec. IV D.

The previous discussion and conclusions apply equally well to the analysis of resonant breakup reactions at 26 and 28 MeV. For the sub-barrier energies (the energy range at which the direct breakup component could be discriminated), Fig. 9(b) shows a similar analysis and comparison between the experimental and calculated distributions of $\theta_{\rm Li}$. For the calculations we have assumed in this case that the weights of the direct and resonant components are those deduced from Fig. 8(b).

D. Breakup emission angles

The last aspect related to the full experimental characterization of breakup reactions is the intrinsic 3D angular distribution of the breakup fragments in their own center-of-mass system. This comprises the polar and azimuthal breakup emission angles $\theta_{d-\alpha}$ and $\phi_{d-\alpha}$ shown in Fig. 3. These variables were obtained from the event-by-event data using the following expressions [28,29]:

$$\begin{aligned}\mathbf{V}_{\rm Li} \cdot \mathbf{V}_{d-\alpha} &= V_{\rm Li} V_{d-\alpha} \cos(\theta_{d-\alpha}) \\ &\quad (\mathbf{V}_{\rm c.m.} \times \mathbf{V}_{\rm Li}) \cdot (\mathbf{V}_d \times \mathbf{V}_{\rm Li}) \\ &= V_{\rm c.m.} V_d V_{\rm Li}^2 \sin(\theta_{\rm Li}) \sin(\theta_{d-\alpha}) \cos(\phi_{d-\alpha}), \\ &\quad (\mathbf{V}_{\rm c.m.} \times \mathbf{V}_{\rm Li}) \times (\mathbf{V}_d \times \mathbf{V}_{\rm Li}) \cdot \mathbf{V}_{\rm Li} \\ &= V_{\rm c.m.} V_d V_{\rm Li}^3 \sin(\theta_{\rm Li}) \sin(\theta_{d-\alpha}) \sin(\phi_{d-\alpha}). \quad (7)\end{aligned}$$

The raw data used in the experimental determination of the intrinsic breakup emission angles have been collected using either in-plane configurations (the two telescopes and

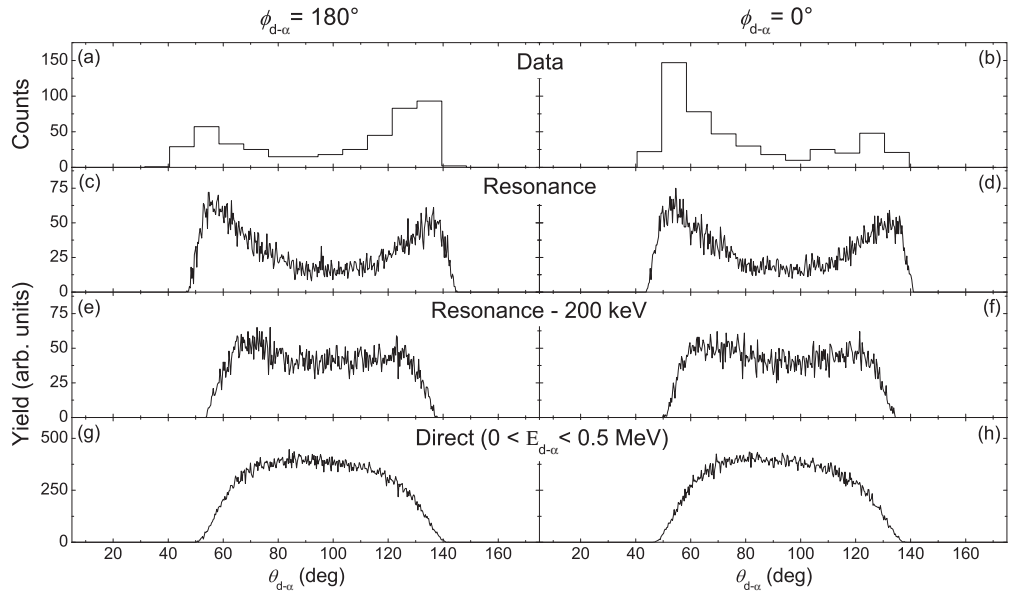

FIG. 10. Experimental [(a) and (b)] and calculated [(c) to (h)] in-plane distributions of breakup emission angles $\theta_{d-\alpha}$ at $E_{\rm lab} = 30$ MeV, $\theta_1 = 92^\circ$, and $\theta_2 = 108.5^\circ$. The comparison between the data and the calculations that have been done assuming different relative-energy distributions reinforces the evidence for the dominant resonant character of the ^{6}Li$\rightarrow d+\alpha$ breakup channel above the barrier and indicates the anisotropy of the emission.

the beam direction lying on the same plane) or the out-of-plane configurations (the plane determined by any telescope and the beam direction does not contain the other telescope). From the definition of the variables and from Fig. 3 it can be inferred that in-plane measurements actually provide information at two azimuthal angles: $\phi_{d-\alpha} = 0^\circ$ and $\phi_{d-\alpha} = 180^\circ$ depending on which particular telescope is hit by either the deuterons or the α particles.

Figure 10 illustrates the typical analysis of an in-plane measurement in terms of the resulting distributions of the intrinsic polar angle $\theta_{d-\alpha}$. The left (right) panels correspond to the detection of deuterons (α particles) in the most forward telescope. The upper row [Figs. 10(a) and 10(b)] displays the experimental distributions which have been obtained by imposing appropriate gating conditions on the two-dimensional ΔE-E spectra. These angular spectra present well-defined bumps centered at approximately 30° and 130° which, as already observed in Sec. IV C, differ noticeably from each other in their intensities. This fact suggests the existence of a marked intrinsic anisotropy in the in-plane emission of the breakup fragments. The corresponding calculated distributions obtained under the assumption of sequential breakup are shown in Figs. 10(c) and 10(d). It can be seen that they are in very good agreement with the data except for the observed anisotropy.

The bottom two rows of Fig. 10 can be used to evaluate the sensitivity of these measurements of $\theta_{d-\alpha}$ when used as a tool to indirectly determine the relative-energy distributions. For example, Figs. 10(e) and 10(f) show the results of a calculation that assumes a narrow distribution, similar to that used to describe the 3^+ resonance in ^{6}Li but arbitrarily centered at an energy 200 keV lower than the resonance energy. This relatively small shift in relative energy produces a significant change in the shape of the calculated distribution, thus making it differ substantially from the shape of the data. As might be expected, an even much more pronounced disagreement is obtained (not shown) if one calculates another real resonance of ^{6}Li such as the 2^+ state located at 4.31 MeV. Finally, the last row [Figs. 10(g) and 10(h)] shows the intrinsic polar angle spectra predicted for an eventual direct-breakup component such as the one that we have observed at the two lowest bombarding energies (schematically described as a uniform relative-energy distribution extending up to 0.5 MeV). Again, it is apparent that under such assumption the shapes of the calculated and experimental angular distributions differ markedly at this higher bombarding energy.

In summary it has been shown that the analysis of the experimental intrinsic angular variables of the breakup emission provides a very selective tool for the discrimination of basic properties such as the resonant or direct character of the reaction. However, the main result that should be directly obtained from these variables is the understanding of the spatial emission pattern of the breakup fragments. This issue will be further discussed in connection with the determination of absolute cross sections.

E. Absolute noncapture breakup cross sections

Differential cross sections $d^2\sigma/d\Omega_{d-\alpha}d\Omega_{\rm Li}$ have been obtained through the application of the procedure described in Sec. III C. For the input to the calculations of the required geometrical efficiencies in Eq. (2) we have taken into account two results that have been discussed in the previous subsections. One of them is the dominance of reactions leading to null or small excitations energies of the final products, i.e., $Q = Q_{\rm gg}$. The other one is related to the distributions of relative energies.

TABLE I. Approximate values and ranges of the center-of-mass angles corresponding to the measurements of direct (D) and resonant (R) breakup reported in the present work. The variations in the ranges of the breakup angles $\theta_{d-\alpha}$ when comparing both processes and/or as a function of $E_{\rm lab}$ are due to the complex geometrical efficiencies of the different telescope configurations for each case. As indicated, these ranges do not depend on the variables $\theta_{\rm Li}$ and $\phi_{d-\alpha}$.

$E_{\rm lab}$ (MeV)	$\theta_{\rm Li}$(deg)	$\theta_{d-\alpha}$(deg)	$\phi_{d-\alpha}$(deg)	Resonant/Direct
30	52.4, 58.0, 60.0, 65.7, 67.7, 73.4, 78.0, 83.5, 85.5, 91.1, 93.0, 98.5, 99.1, 105.1, 108.0, 113.2, 115.3, 120.7	45–145	0, 180	R
	98.1	50–130	14, 24, 37, 46, 51	R
	104.0	50–130	194, 204, 217, 226, 233	R
28	47.7, 52.4, 57.3, 63.0, 65.2, 70.8, 73.5, 81.0, 85.5, 91.1, 93.4, 99.4, 108.0, 113.4, 117.8, 123.0, 125.0, 130.4	45–145	0, 180	R
26	70.4, 75.9, 78.0, 83.5, 85.5, 91.1, 93.2, 98.3, 100.0, 105.5, 107.8, 113.2, 115.2, 120.5	45–145	0, 180	R
24	85.5, 91.1, 93.1, 98.5, 100.0, 105.7, 108.0, 113.2	40–70/120–150	0, 180	R
		60–130	0, 180	D
23	100.0, 105.0	40–70/120–150	0, 180	R
		60–130	0, 180	D

As discussed before, we have assumed a single uniform narrow component centered at $E_{d-\alpha} = 0.71$ MeV and a width of 0.10 MeV for the case of resonant breakup and a wide uniform distribution that extends to 0.5 MeV for the case of direct breakup. Table I summarizes the approximate center-of-mass angular values and ranges that have been covered by the present measurements, as a result of the different geometrical configurations of the two telescopes. Figure 11 shows a few examples of the experimental differential cross sections of resonant breakup as a function of the intrinsic polar angle $\theta_{d-\alpha}$ for three of the bombarding energies at $\theta_{\rm Li} \approx 103^\circ$ (23 MeV) and 81° (26 and 30 MeV) and at two fixed values of the azimuthal angle: $\phi_{d-\alpha} = 0^\circ$ [deuteron detected by telescope 2; Figs. 11(a), 11(c) and 11(e)] and $\phi_{d-\alpha} = 180^\circ$ [deuteron detected by telescope 1; Figs. 11(b), 11(d), and 11(f)]. These cases correspond to the in-plane measurements. The observed trend, especially at 26 and 30 MeV, confirms the rather marked asymmetry that had been anticipated in the previous subsection, with probabilities of emission that peak at $\theta_{d-\alpha} = 60^\circ$ and 120°, respectively. A similar asymmetric behavior, at least for the measurements at $E_{\rm lab} \geqslant 26$ MeV, has been observed for all the values of $\theta_{\rm Li}$ that have been obtained by varying the angular positions of the two telescopes and also at the out-of-plane measurements. As exemplified in the bottom row of Fig. 11, it is not possible to draw a definite conclusion regarding this asymmetry at the lowest energies (23 and 24 MeV) because of the lack of data points in the relevant angular region (approximately 50° to 130°), where the geometrical efficiency for the detection of resonant breakup is too low.

It may be worthwhile to attempt a visualization of the emission pattern and the conditions for enhanced or hindered in-plane emission that correspond to the distributions of Fig. 11. Taking into account the meaning of the angular variable $\theta_{d-\alpha}$ (see Fig. 3) the results can be geometrically interpreted with the aid of the schematic diagram shown in Fig. 12. According to this diagram, the center-of-mass. directions of emission of in-plane deuterons and α particles can be qualitatively classified taking as a reference the velocity vector of the projectile ("beam direction") and the asymptotic center-of-mass velocity vector of the binary ejectile, $\mathbf{V}_{\rm Li}$. In the first place, the emission of the light particle "x" can be classified as (1) *forward* (checkered symbols) or (2) *backward* (plain symbols) with respect to $\mathbf{V}_{\rm Li}$. In either case the classification must be completed by stating whether this particle "x" flies (a) *towards* or (b) *away* from the beam

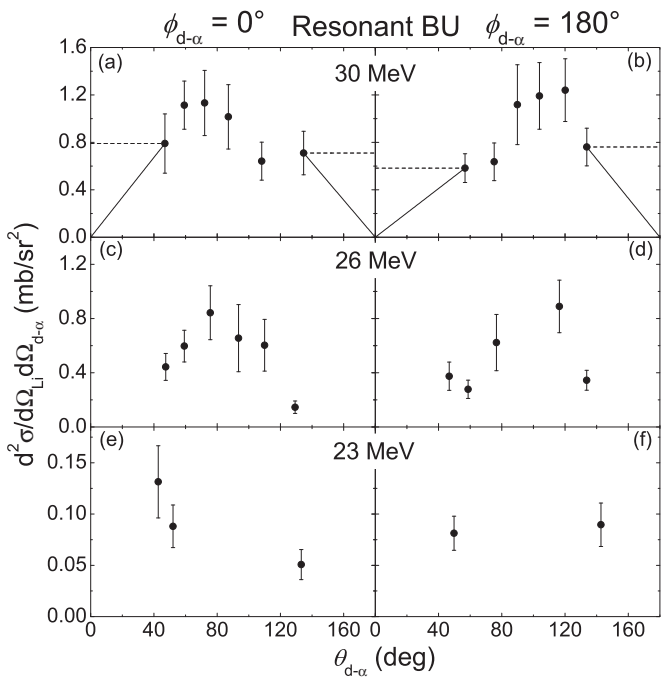

FIG. 11. Differential cross sections for resonant breakup as a function of the center-of-mass polar angle for d-α emission at three values of $E_{\rm lab}$. The two groups correspond to values of approximately 0° [(a), (c), and (e)] and 180° [(b), (d), and (f)] of the azimuthal angle. The solid and dashed curves at 30 MeV illustrate the two extrapolations that have been used for the numerical integration outside the measured range in order to estimate the uncertainty in the extraction of $d\sigma/d\Omega_{\rm Li}$.

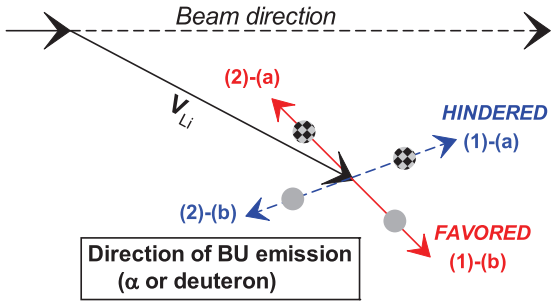

FIG. 12. (Color online) Schematic diagram that illustrates the conditions for enhanced or hindered in-plane emission corresponding to typical $\theta_{d-\alpha}$ distributions, such as those shown in Fig. 11. See text for details.

direction (which, in terms of laboratory angles, corresponds to the conditions $\theta_x < \theta_{\rm Li}$ and $\theta_x > \theta_{\rm Li}$, respectively). Using this classification, it can finally be said that our results show an emission of deuterons or α particles which is enhanced in the configuration (2)-(a) [equivalent to (1)-(b)] and hindered for (1)-(a) [equivalent to (2)-(b)]. A similar finding has been reported by Santra *et al.* [20] for the ^{6}Li+^{209}Bi system based on the observation of different peak intensities in the energy spectra of the deuterons and α particles emitted in that reaction. It can be demonstrated that the qualitative pattern that emerges from Ref. [20] agrees with the present results, although in our case they are based on the analysis of the relevant variables (the center-of-mass breakup-emission angles) and therefore furnish a more direct geometric interpretation of the problem.

Figure 13 shows some of the spectra taken under conditions similar to those of Fig. 11, but in this case corresponding to nonresonant breakup at sub-barrier energies. In spite of the limited range resulting from the geometrical efficiency for these reactions and the statistical uncertainties, the results seem to be in all cases consistent with isotropic distributions.

Regarding the out-of-plane measurements (i.e., values of $\phi_{d-\alpha}$ other than 0° or 180° at fixed values of $\theta_{\rm Li}$), representative results for resonant breakup are shown in Fig. 14. Again, no significant anisotropies are observed over the measured ranges within statistical errors.

The experimental differential cross sections obtained from all the measurements listed in Table I have been numerically integrated over 4π sr in the breakup solid angle $\Omega_{d-\alpha}$ to obtain $d\sigma/d\Omega_{\rm Li}$. Whenever extrapolations or interpolations were necessary, we have used the information previously discussed in relation to Figs. 11, 13, and 14. Two different extrapolations of the polar-angle data have been used to estimate the contributions from the unmeasured angular ranges in the vicinity of $\theta_{d-\alpha} = 0°$ and 180°, which are illustrated by the straight segments shown in the 30 MeV spectra of Fig. 11. One of these extrapolations is based on linear functions that vanish at those extreme angles (solid segments) while the other assumes constant values equal to those of the most forward and backward measured points (dashed segments). It was observed that both extrapolations yielded similar results. Finally, the first case was used for the calculations while the differences among them were taken as an additional factor contributing to the uncertainties of the integrals.

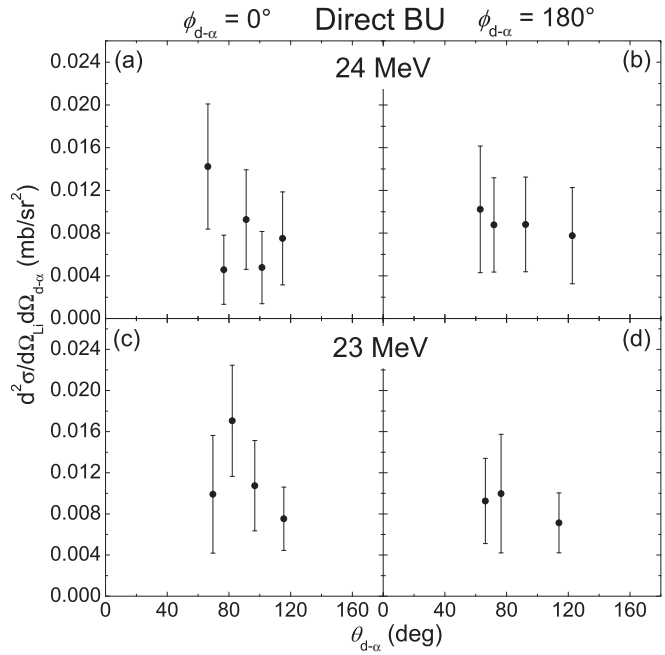

FIG. 13. Differential cross sections for direct (nonresonant) breakup as a function of the center-of-mass polar angle for d-α emission at sub-barrier energies. The two groups correspond to values of approximately 0° [(a) and (c)] and 180° [(b) and (d)] of the azimuthal angle.

According to the results of the out-of-plane measurements we have considered azimuthal symmetry for all cases, i.e., no dependence of $d^2\sigma/d\Omega_{d-\alpha}d\Omega_{\rm Li}$ on $\phi_{d-\alpha}$. Table II summarizes the differential breakup cross sections obtained as a result of this procedure for both resonant and direct processes as a function of the bombarding energy. As an example of these angular distributions, Fig. 15 shows the results obtained at 30 MeV normalized to Rutherford cross sections. For the purpose of comparison among different reaction channels, the figure also includes the normalized values of the cross sections for elastic and inelastic scattering reported for this same system in Refs. [34,35], respectively. Within statistical uncertainties the probability of occurrence is approximately

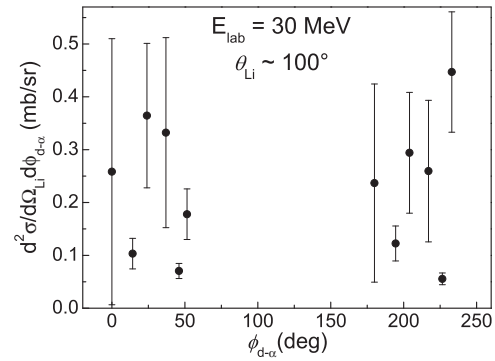

FIG. 14. Differential cross sections for resonant breakup as a function of the center-of-mass azimuthal angles for d-α emission at $E_{\rm lab} = 30$ MeV and $\theta_{\rm Li} \approx 100°$. See text for details.

TABLE II. Differential cross sections $d\sigma/d\Omega_{\rm Li}$ for resonant and non-resonant breakup into d-α as a function of the c.m. binary angle and bombarding energy. For the highest energies (26, 28 and 30 MeV) the non-resonant component could not be identified due to experimental constraints.

$E_{\rm lab} = 30$ MeV		$E_{\rm lab} = 28$ MeV		$E_{\rm lab} = 26$ MeV	
$\theta_{\rm Li}$(deg)	$d\sigma/d\Omega_{\rm Li}$(mb/sr) Resonant	$\theta_{\rm Li}$(deg)	$d\sigma/d\Omega_{\rm Li}$(mb/sr) Resonant	$\theta_{\rm Li}$(deg)	$d\sigma/d\Omega_{\rm Li}$(mb/sr) Resonant
52.4	17.8 ± 5.4	47.7	14.6 ± 7.7	70.4	7.8 ± 2.3
58.0	13.0 ± 4.7	52.4	16.7 ± 11.0	75.9	5.9 ± 1.7
60.0	12.5 ± 2.9	57.3	5.0 ± 1.9	78.0	5.9 ± 1.7
65.7	12.2 ± 2.7	63.0	4.2 ± 1.7	83.5	6.0 ± 1.7
67.7	12.0 ± 3.1	65.2	8.6 ± 4.4	85.5	5.8 ± 1.9
73.4	14.9 ± 4.0	70.8	6.2 ± 3.9	91.1	3.6 ± 1.3
78.0	9.6 ± 2.6	73.5	5.8 ± 3.5	93.2	4.1 ± 2.1
83.5	9.8 ± 2.5	81.0	6.0 ± 3.0	98.3	4.2 ± 1.8
85.5	6.4 ± 2.3	85.5	7.2 ± 3.2	100.0	1.2 ± 0.5
91.1	4.0 ± 1.9	91.1	6.6 ± 3.0	105.5	1.3 ± 0.4
93.0	10.1 ± 4.5	93.4	2.4 ± 1.1	107.8	1.8 ± 0.5
98.5	7.3 ± 3.6	99.4	2.4 ± 1.0	113.2	1.6 ± 0.5
99.1	1.6 ± 1.6	108.0	3.1 ± 1.4	115.2	1.7 ± 0.5
105.1	1.5 ± 1.2	113.4	2.9 ± 1.2	120.5	1.3 ± 0.4
108.0	2.2 ± 0.8	117.8	6.2 ± 1.5		
113.2	1.8 ± 0.7	123.0	4.9 ± 1.4		
115.3	2.1 ± 1.0	125.0	4.5 ± 1.2		
120.7	1.2 ± 0.6	130.4	3.4 ± 1.1		

$E_{\rm lab} = 24$ MeV			$E_{\rm lab} = 23$ MeV		
$\theta_{\rm Li}$(deg)	$d\sigma/d\Omega_{\rm Li}$(mb/sr) Resonant	$d\sigma/d\Omega_{\rm Li}$(mb/sr) Direct	$\theta_{\rm Li}$(deg)	$d\sigma/d\Omega_{\rm Li}$(mb/sr) Resonant	$d\sigma/d\Omega_{\rm Li}$(mb/sr) Direct
85.5	3.9 ± 1.2	0.35 ± 0.15	100.0	0.7 ± 0.2	0.11 ± 0.04
91.1	3.1 ± 1.0	0.26 ± 0.11	105.0	0.8 ± 0.2	0.08 ± 0.04
93.1	3.8 ± 1.2	0.42 ± 0.20			
98.5	2.4 ± 1.0	0.40 ± 0.17			
100.0	2.4 ± 1.0	0.14 ± 0.09			
105.7	1.7 ± 1.1	0.13 ± 0.08			
108.0	0.9 ± 0.3	0.11 ± 0.06			
113.2	0.7 ± 0.3	0.10 ± 0.05			

5 times larger for breakup than for inelastic scattering over the entire measured angular range. For both channels a rather flat maximum is observed at values in the vicinity of the calculated grazing angle, which is indicated in the figure by the vertical arrow. The dashed curve that describes the elastic-scattering data is based on a parameter-free optical model calculation that takes the breakup channel into account [36,37]. The solid curve shown in the same figure corresponds to calculations of the noncapture breakup channel based on the classical dynamical description of Diaz-Torres [26,27]. This model treats projectile breakup as a stochastic process and evaluates the subsequent fate of the products according to various conditions at the moment at which breakup occurs. In this way noncapture breakup, incomplete fusion or complete fusion following breakup can be obtained depending on whether both fragments manage to fly away, or one or both fragments are absorbed by the target nucleus. The breakup probability $P_{\rm BU}$ for a fixed energy and impact parameter is given by $P_{\rm BU} = \exp(-\alpha R_{\rm min} + \beta)$, where $R_{\rm min}$ is defined as the barrier radius if the partial wave is lower than the critical angular momentum associated to complete fusion, and as D (the distance of closest approach for a Coulomb trajectory) otherwise. The calculations have been done using the code PLATYPUS [38]. The values of the logarithmic slope α and the intercept β that we have chosen for its application to a ^{6}Li projectile were 0.280 fm^{-1} and 0.661, respectively. These values were extracted from the present measurements performing an exponential least-squares fit to the differential resonant noncapture breakup cross sections (shown in Fig. 16 as a function of the distance of closest approach, D) disregarding the contribution of the direct component. Other elements used in the calculations were the nuclear parameters for the Woods-Saxon potentials which were taken from the systematics of Broglia and Winther [39,40]. The solid curve in Fig. 15 that results from these calculations qualitatively reproduces the trend of the data points for resonant breakup, including the peaking near the grazing angle. Regarding this comparison, it should be kept in mind that the distinction between resonant and nonresonant breakup is beyond the reach of the model.

The peripheral character of these reactions can be better evaluated by displaying the normalized cross sections as a function of the distance of closest approach (D). Under the

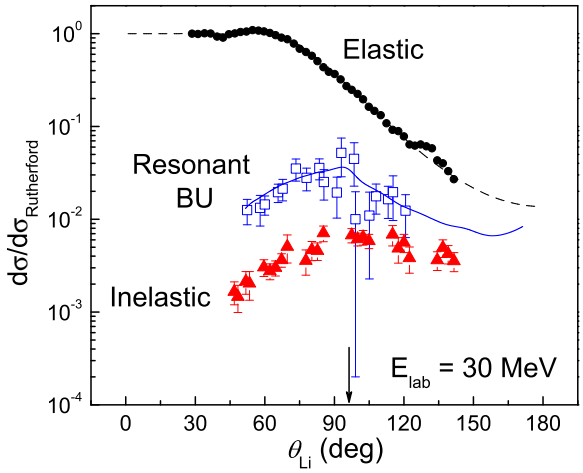

FIG. 15. (Color online) Differential cross sections for resonant breakup (this work), elastic scattering [34], and inelastic scattering [35] as a function of the center-of-mass binary angle, normalized to Rutherford cross sections at $E_{\rm lab} = 30$ MeV, the vertical arrow indicates the grazing angle. The labels indicate the groups of data points corresponding to each one of those channels. The solid curve is a prediction for the noncapture breakup channel applying the model of Refs. [26,27]. The dashed curve is a calculation based on the model of Refs. [36,37]. See text for details.

assumption of Coulomb scattering, this is done in Fig. 16 which now includes the data for all the bombarding energies for resonant and direct breakup, as well as preexistent elastic [34] and inelastic-scattering data [35] for the same system. The behavior of the resonant breakup data at the largest calculated distances considering all the energies can be approximately described by an exponential decay with a constant of -0.28 fm^{-1}. On other hand, the data points for direct breakup appear at distances around and above 13 fm; this observation tentatively supports a connection that has been proposed between low relative energies and breakup taking place at long distances [24]. However, a more definite conclusion in this respect would require further direct breakup data at higher bombarding energies and with better efficiency. The qualitatively similar exponential behavior that has been observed for distant transfer reactions [41,42] is usually interpreted as arising from quantum tunneling of the transferred particle through a potential barrier. In the case of transfer, the slopes of the exponential tails obtained in this way present a marked dependence upon the energy, although this dependence has in turn been shown to largely disappear if one introduces a more realistic calculation of the internuclear distances and takes the absorption into account [43]. In the case of breakup, and depending on the exact mechanism that governs the partition and emission of the breakup fragments in the short distance domain where the reaction takes place, it might also be argued that the asymptotic relation between the binary scattering angle and the internuclear distance is not so well defined. In addition, for the present breakup data the magnitude of the experimental uncertainties makes it difficult to establish clear trends and thus to undertake a more refined analysis along these lines.

Finally, total breakup cross sections have been obtained by numerical integration of the experimental values of $d\sigma/d\Omega_{\rm Li}$ over 4π sr in binary solid angle, applying a prescription similar to the one described above for the extrapolation to the most forward and backward angles. The results for resonant and direct breakup into d-α mode are presented in Fig. 17, which, for comparison, also includes the cross sections for complete fusion reported by Rath *et al.* [44]. The solid curve shows the predictions of the dynamical classical model of Diaz-Torres

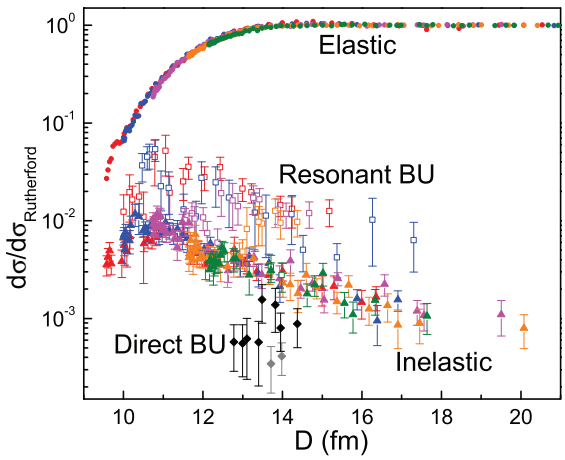

FIG. 16. (Color online) Differential cross sections for resonant and direct breakup into d-α partition (this work), elastic scattering [34], and inelastic scattering [35] normalized to Rutherford cross sections as a function of the distance of closest approach (D). The labels indicate the groups of data points corresponding to each one of those channels. The different colors correspond to each one of the bombarding energies used in the measurements of noncapture breakup in the present work.

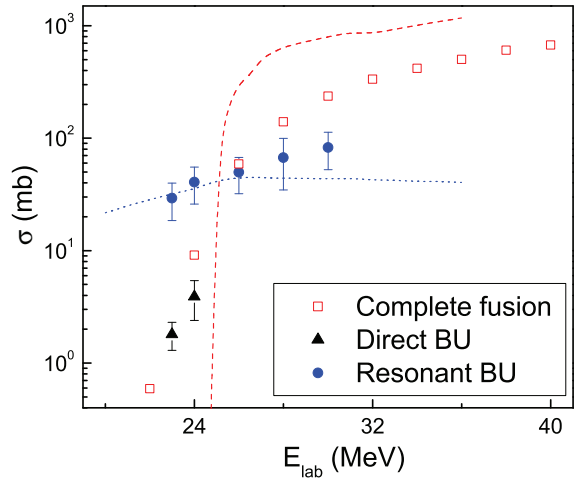

FIG. 17. (Color online) Total cross sections for resonant and nonresonant breakup into d-α mode (this work) and complete fusion [44] as a function of the bombarding energy. The labels indicate the groups of data points corresponding to each one of those channels. The solid and dashed curves are predictions of the noncapture breakup channel and of fusion, respectively, applying the model of Refs. [26,27]. See text for details.

[26] for the noncapture breakup channel. As has already been shown for the case of the binary angular distributions, the model succeeds in the quantitative description of the experimental behavior of the resonant noncapture breakup data as a function of energy. Actually, one can also conclude that the agreement would still very reasonable even if the relatively minor contribution of the direct breakup cross sections that could be measured at the lowest energies were to be added. However, it is difficult to draw a more definite conclusion in this respect at the moment since it has not been possible to measure the direct breakup channel over the whole energy range. The predictions of the same calculation for the complete fusion cross sections are shown by the dashed curve; in this case, the energies are restricted to the above-barrier range given the classical character of the model. The comparison between the experimental cross sections for both reaction channels point to an increasing dominance of noncapture breakup over fusion as the energy decreases below the barrier.

V. SUMMARY AND CONCLUSIONS

Noncapture breakup reactions induced by weakly bound ^{6}Li projectiles on a ^{144}Sm target have been investigated at five bombarding energies close to the Coulomb barrier through the correlated detection of the emitted light particles. The body of analyzed results comprises all those reactions that result in the breakup of the ^{6}Li projectile into a deuteron and an α particle (we leave aside for a forthcoming publication the analysis of other complex and less intense reaction channels). The breakup mode has been first identified and then fully characterized on the basis of a complete set of variables adequately chosen to provide the most physically significant description of the system directly obtainable from the data in a model-independent way. At each energy, the angular measurements cover both the binary-reaction angle (the asymptotic emission angle of the virtual binary ejectile) and the breakup angles (the asymptotic in-plane and out-of-plane emission angles of the light fragments in the ejectile frame). The geometry of the detection system has been considered in detail for the computation of the efficiency of the coincident measurements and for the extraction of the corresponding differential and integrated cross sections.

The first common experimental result for the α-deuteron breakup mode obtained from the three-body kinematics relates to the dominant population of the ground states and, probably, of the lowest excited states of the ^{144}Sm target nucleus. The obtained experimental distributions of other relevant variables, such as the kinetic energies of the breakup fragments in the ejectile center-of-mass reference frame conveys decisive information to establish the resonant or direct (nonresonant) character of the reactions. In the particular case of this variable the identification of each one of these processes can be achieved in an indirect although very selective manner. The validity of the results could be independently confirmed through the analysis of the shapes of the intrinsic breakup angular distributions. In this way it could be determined that for the projectile breakup channel the resonant process that involves the lowest-lying 3^{+} state of ^{6}Li dominates at all energies, although, due to the peculiarities of the detection system, the direct-to-resonant ratio could only be quantitatively measured at the sub-barrier energies and found to be around 10%. In spite of the expected very high selectivity of the detection system for the identification of higher resonances, no statistically significant evidence of such processes was found.

In accordance with the results of previous works, the breakup polar-angle distributions exhibit a quite marked anisotropy that involves, as references, the beam direction and the asymptotic emission direction of the binary virtual ejectile. These two directions also define the plane that is taken in turn as reference for the breakup azimuthal-angle distributions, obtained from the out-of-plane measurements. Within experimental uncertainties and to the extent of the covered angular regions, we conclude that the out-of-plane results are consistent with uniform distributions.

The probabilities for breakup emission as a function of the asymptotic binary scattering angles have been analyzed in terms of the minimum internuclear distances between projectile and target obtained under the assumption of Coulomb trajectories. In spite of the relatively large experimental fluctuations that somehow blur the conclusions, the results for internuclear distances larger than the corresponding value to the grazing angle follow a slow, approximately exponential, decrease with no apparent energy dependence such as that observed in some transfer reactions. The total cross section for resonant breakup of ^{6}Li equals the complete fusion cross section at approximately the barrier energy and becomes the dominant channel as the energy decreases towards the sub-barrier region, where we have found an additional contribution of about 10% from nonresonant processes. The experimental differential and integrated cross sections obtained in this work have been compared to the cross sections of other channels previously measured for the same system and to the results of calculations based on a dynamic classical description of breakup, incomplete fusion, and complete fusion in reactions induced by weakly bound projectiles.

[1] G. Baur, F. Rösel, D. Trautmann, and R. Shyam, Phys. Rep. **111**, 333 (1984).
[2] D. L. Disdier, G. C. Ball, O. Häusser, and R. E. Warner, Phys. Rev. Lett. **27**, 1391 (1971).
[3] J. L. Québert, B. Frois, L. Marquez, G. Sousbie, R. Ost, K. Bethge, and G. Gruber, Phys. Rev. Lett. **32**, 1136 (1974).
[4] R. Ost, E. Speth, K. O. Pfeiffer, and K. Bethge, Phys. Rev. C **5**, 1835 (1972).
[5] D. Scholz, H. Gemmeke, L. Lassen, R. Ost, and K. Bethge, Nucl. Phys. A **288**, 351 (1977).
[6] M. Dasgupta, P. R. S. Gomes, D. J. Hinde, S. B. Moraes, R. M. Anjos, A. C. Berriman, R. D. Butt, N. Carlin, J. Lubian, C. R.

Morton, J. O. Newton, and A. Szanto de Toledo, Phys. Rev. C **70**, 024606 (2004).
[7] J. Kolata, Eur. Phys. J. A **13**, 117 (2002).
[8] C. Beck, F. A. Souza, N. Rowley, S. J. Sanders, N. Aissaoui, E. E. Alonso, P. Bednarczyk, N. Carlin, S. Courtin, A. Diaz-Torres, A. Dummer, F. Haas, A. Hachem, K. Hagino, F. Hoellinger, R. V. F. Janssens, N. Kintz, R. Liguori Neto, E. Martin, M. M. Moura, M. G. Munhoz, P. Papka, M. Rousseau, A. Sànchez i Zafra, O. Stézowski, A. A. Suaide, E. M. Szanto, A. Szanto de Toledo, S. Szilner, and J. Takahashi, Phys. Rev. C **67**, 054602 (2003).
[9] C. H. Dasso and R. Donangelo, Phys. Lett. B **276**, 1 (1992).
[10] K. Hagino, A. Vitturi, C. H. Dasso, and S. M. Lenzi, Phys. Rev. C **61**, 037602 (2000).
[11] M. S. Hussein, M. P. Pato, L. F. Canto, and R. Donangelo, Phys. Rev. C **46**, 377 (1992).
[12] K. Rusek, N. Alamanos, N. Keeley, V. Lapoux, and A. Pakou, Phys. Rev. C **70**, 014603 (2004).
[13] L. F. Canto, P. R. S. Gomes, R. Donangelo, and M. S. Hussein, Phys. Rep. **424**, 1 (2006).
[14] G. Baur, C. A. Bertulani, and H. Rebel, Nucl. Phys. A **458**, 188 (1986).
[15] Y. Tokimoto, H. Utsunomiya, T. Yamagata, M. Ohta, Y. W. Lui, R. P. Schmitt, S. Typel, Y. Aoki, K. Ieki, and K. Katori, Phys. Rev. C **63**, 035801 (2001).
[16] H. Utsunomiya, Y. W. Lui, D. R. Haenni, H. Dejbakhsh, L. Cooke, B. K. Srivastava, W. Turmel, D. O'Kelly, R. P. Schmitt, D. Shapira, J. Gomez del Campo, A. Ray, and T. Udagawa, Phys. Rev. Lett. **65**, 847 (1990).
[17] R. J. de Meijer and R. Kamermans, Rev. Mod. Phys. **57**, 147 (1985).
[18] S. B. Gazes, J. E. Mason, R. B. Roberts, and S. G. Teichmann, Phys. Rev. Lett. **68**, 150 (1992).
[19] J. Hesselbarth and K. T. Knöpfle, Phys. Rev. Lett. **67**, 2773 (1991).
[20] S. Santra, V. V. Parkar, K. Ramachandran, U. K. Pal, A. Shrivastava, B. J. Roy, B. K. Nayak, A. Chatterjee, R. K. Choudhury, and S. Kailas, Phys. Lett. B **677**, 139 (2009).
[21] K. Pfeiffer, E. Speth, and K. Bethge, Nucl. Phys. A **206**, 545 (1973).
[22] R. Ost, K. Bethge, H. Gemmeke, L. Lassen, and D. Scholz, Zeitschr. Phys. **266**, 369 (1974).
[23] A. Shrivastava, A. Navin, N. Keeley, K. Mahata, K. Ramachandran, V. Nanal, V. V. Parkar, A. Chatterjee, and S. Kailas, Phys. Lett. B **633**, 463 (2006).
[24] D. H. Luong, M. Dasgupta, D. J. Hinde, R. du Rietz, R. Rafiei, C. J. Lin, M. Evers, and A. Diaz-Torres, Phys. Lett. B **695**, 105 (2011).
[25] D. H. Luong, M. Dasgupta, D. J. Hinde, R. du Rietz, R. Rafiei, C. J. Lin, M. Evers, and A. Diaz-Torres, Phys. Rev. C **88**, 034609 (2013).
[26] A. Diaz-Torres, D. J. Hinde, J. A. Tostevin, M. Dasgupta, and L. R. Gasques, Phys. Rev. Lett. **98**, 152701 (2007).
[27] A. Diaz-Torres, J. Phys. G: Nucl. Part. Phys. **37**, 075109 (2010).
[28] D. Martinez Heimann, A. J. Pacheco, and O. A. Capurro, Nucl. Instrum. Methods A **622**, 642 (2010).
[29] D. Martinez Heimann, A. J. Pacheco, and O. A. Capurro, Nucl. Instrum. Methods A **694**, 313 (2012).
[30] G. G. Ohlsen, Nucl. Instrum. Methods **37**, 240 (1965).
[31] J. J. Kolata, H. Amro, F. D. Becchetti, J. A. Brown, P. A. DeYoung, M. Hencheck, J. D. Hinnefeld, G. F. Peaslee, A. L. Fritsch, C. Hall, U. Khadka, P. J. Mears, P. O'Rourke, D. Padilla, J. Rieth, T. Spencer, and T. Williams, Phys. Rev. C **75**, 031302 (2007).
[32] F. Souza, C. Beck, N. Carlin, N. Keeley, R. L. Neto, M. de Moura, M. Munhoz, M. D. Santo, A. Suaide, E. Szanto, and A. S. de Toledo, Nucl. Phys. A **821**, 36 (2009).
[33] A. B. McIntosh, S. Hudan, C. J. Metelko, R. T. de Souza, R. J. Charity, L. G. Sobotka, W. G. Lynch, and M. B. Tsang, Phys. Rev. Lett. **99**, 132701 (2007).
[34] J. M. Figueira, J. O. Fernández Niello, A. Arazi, O. A. Capurro, P. Carnelli, L. Fimiani, G. V. Martí, D. Martinez Heimann, A. E. Negri, A. J. Pacheco, J. Lubian, D. S. Monteiro, and P. R. S. Gomes, Phys. Rev. C **81**, 024613 (2010).
[35] A. E. Woodard, J. M. Figueira, D. R. Otomar, J. O. Fernández Niello, J. Lubian, A. Arazi, O. A. Capurro, P. Carnelli, L. Fimiani, G. V. Martí, D. Martinez Heimann, D. S. Monteiro, A. E. Negri, A. J. Pacheco, and P. R. S. Gomes, Nucl. Phys. A **873**, 17 (2012).
[36] D. Pereira, J. Lubian, J. R. B. Oliveira, D. P. de Sousa, and L. C. Chamon, Phys. Lett. B **670**, 330 (2009).
[37] D. P. Sousa, D. Pereira, J. Lubian, L. C. Chamon, J. R. B. Oliveira, E. S. Rossi, Jr., C. P. Silva, P. N. de Faria, V. Guimarães, R. Lichtenthaler, and M. A. G. Alvarez, Nucl. Phys. A **836**, 1 (2010).
[38] A. Diaz-Torres, Comput. Phys. Commun. **182**, 1100 (2011).
[39] W. Reisdorf, J. Phys. G: Nucl. Part. Phys. **20**, 1297 (1994).
[40] I. Dutt and R. K. Puri, Phys. Rev. C **81**, 064609 (2010).
[41] A. O. Macchiavelli, M. A. Deleplanque, R. M. Diamond, F. S. Stephens, E. L. Dines, and J. E. Draper, Nucl. Phys. A **432**, 436 (1985).
[42] D. Tomasi, J. O. Fernández Niello, A. J. Pacheco, D. Abriola, J. E. Testoni, A. O. Macchiavelli, O. A. Capurro, D. E. DiGregorio, M. di Tada, G. V. Martí, and I. Urteaga, Phys. Rev. C **54**, 1282 (1996).
[43] H. D. Marta, R. Donangelo, D. Tomasi, J. O. Fernández Niello, and A. J. Pacheco, Phys. Rev. C **54**, 3156 (1996).
[44] P. K. Rath, S. Santra, N. L. Singh, R. Tripathi, V. V. Parkar, B. K. Nayak, K. Mahata, R. Palit, S. Kumar, S. Mukherjee, S. Appannababu, and R. K. Choudhury, Phys. Rev. C **79**, 051601 (2009).